

Layered MXene Protected Lithium Metal Anode as an Efficient Polysulfide Blocker for Lithium-Sulfur Batteries

Wantang Li⁺^[a] Yifang Zhang⁺^[a] Huan Li,^{*[a]} Zijin Chen,^[b] Tongxin Shang,^[a] Zhitan Wu,^[a] Chen Zhang,^[c] Jia Li,^[b] Wei Lv,^[b] Ying Tao,^{*[a]} and Quan-Hong Yang^[a]

The shuttle effect of lithium polysulfides (LiPSs) from sulfur cathode to lithium (Li) anode is one of the main obstacles for lithium-sulfur (Li–S) batteries. The severe corrosion of Li metal anode by the dissolved LiPSs bottlenecks the efficient operation of Li–S batteries, however, the anode part has not been received much attention compared to those extensive efforts related to the cathode designs. Herein, we show that the interface between $Ti_3C_2T_x$ ($T=-OH, -F$)-based MXene and reduced graphene oxide (rGO) is able to guide uniform Li nucleation, promoting highly reversible and dendrite-free Li plating/stripping. Such the Li anode demonstrates excellent

cycling stability for more than 1000 hours even under ultra-high rate (10 mA cm^{-2}) and high areal capacity (3 mAh cm^{-2}). More importantly, the well-designed 2D layered structure by coupling the $Ti_3C_2T_x$ with a graphene scaffold, is highly efficient to block the shuttled polysulfides and inhibit the corrosion of the lithium metal anode. As a result, the Li–S full battery exhibits a stable cycling stability with a high Coulombic efficiency of 99.8% over 300 cycles. This work suggests the design strategy of Li metal anode especially targeting at the sulfur cathode, and we hope it can provide valuable inspirations for the future design of Li metal anodes for more practical Li–S batteries.

1. Introduction

Lithium-sulfur (Li–S) batteries hold great promise among the future energy storage devices due to their theoretically high energy density (2600 Wh kg^{-1}), low cost and environmental friendliness.^[1] However, their practical use in large scales is restricted by many issues such as the poor electrical conductivity of sulfur, solid-state discharge products (Li_2S/Li_2S_2), and the large volume change (~80%) of the sulfur cathode during cycling.^[2] Among these problems, the shuttle effect of lithium polysulfides (LiPSs) from sulfur cathode to lithium (Li) anode is believed as the biggest obstacle, which hinders the practical use of Li–S batteries by the fast capacity decay.^[3] Many efforts have been made to inhibit the shuttle effect by restraining the dissolution of LiPSs from the sulfur cathode.^[4] However, these undertakings fail to entirely confine the LiPSs

on the cathode part, which means that some LiPSs are still likely to shuttle to the anode. The side reactions between LiPSs and Li anode produce the insulating Li_2S_2 and Li_2S solids covered on the Li surface, leading to the passivation of anode and fast battery failure.^[3b,c,5] Different protection schemes have been employed to stabilize the Li metal anode, including electrolyte engineering, 3D Li metal host, artificial solid-electrolyte-interphase, etc.^[6] As a result, excellent cycling stability has been achieved by coupling the Li anodes with those intercalation-type cathodes such as $LiFePO_4$ and $LiCoO_2$.^[7] However, these strategies generally focus on the suppression of Li dendritic structure, but the corrosion of Li anode by LiPSs has not received much attention. Therefore, the Li anode design especially targeting at sulfur cathode remains far from the satisfaction for the practical use of Li–S batteries.

Considering the high specific capacity (1675 mAh g^{-1}) and high charge-discharge current density ($1 \text{ C} \approx 6.7 \text{ mA cm}^{-2}$ with an areal sulfur loading of ~4 mg cm⁻²) of sulfur cathode, those coupled Li anodes are required for excellent stability with high-rate and high-capacity Li plating/stripping abilities.^[3b] Unfortunately, the electrochemical plating/stripping of the state-of-the-art Li anodes is still restricted by the low current densities and areal capacities,^[8] possibly due to a relatively lower criteria of Li anodes for those intercalation-type cathode materials.^[9] For the host design, unimpeded ion transport and high electrical conductivity are favorable to achieve a high-rate stability, and a high specific surface area contributes to a high areal capacity.^[10] In this regard, $Ti_3C_2T_x$ -based MXene is a good choice due to its excellent conductivity and high specific surface area.^[11] More importantly, the amounts of functional groups on the $Ti_3C_2T_x$ are expected to guide uniform Li nucleation and regulate the subsequent Li growth structure. The integration of $Ti_3C_2T_x$ into 3D hosts is widely used to inhibit dendrite growth by obtaining

[a] W. Li,⁺ Dr. Y. Zhang,⁺ H. Li, T. Shang, Z. Wu, Prof. Y. Tao, Prof. Q.-H. Yang
Nanyang Group, State Key Laboratory of Chemical Engineering
School of Chemical Engineering and Technology
Tianjin University, Tianjin 300350, China
E-mail: huan@tju.edu.cn
yingtao@tju.edu.cn

[b] Z. Chen, Prof. J. Li, Prof. W. Lv
Shenzhen Geim Graphene Center
Division of Energy and Environment
Graduate School at Shenzhen
Tsinghua University
Shenzhen 518055, China
[c] Dr. C. Zhang
School of Marine Science and Technology
Tianjin University, Tianjin 300350, China

[+] These authors contributed equally to this work.

 Supporting information for this article is available on the WWW under
<https://doi.org/10.1002/batt.202000062>

 An invited contribution to a Special Collection on Lithium Metal Anode Processing and Interface Engineering

lower local current densities.^[12] However, their 3D opening pore channels deteriorate the reaction between LiPSs and Li anode, whereas 2D structure is more reliable to block the LiPSs and protect Li anode. Consequently, efficient operation of Li anode for Li–S batteries is more challenging because a more comprehensive anode design, considering high current densities, high areal capacities, and the inhabitation of side reactions between LiPSs and Li anode, is needed.

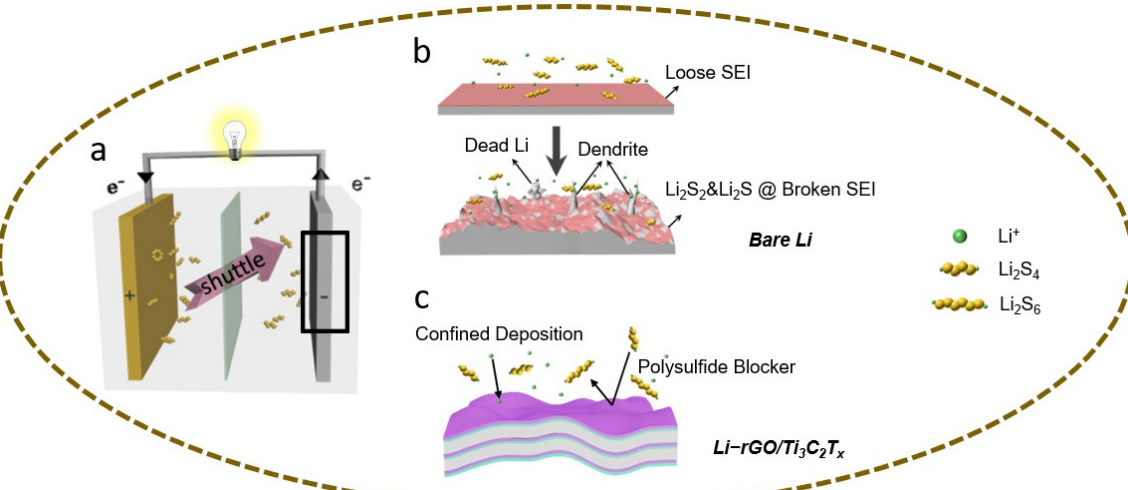
In this work, we present a layered composite anode composed of reduced graphene oxide (rGO) and $Ti_3C_2T_x$ for use as the Li metal host. We have found that the interface between $Ti_3C_2T_x$ and rGO is able to guide uniform Li nucleation and deposition by combining experimental results and theoretical computations. Compared to a conventional Li anode, such the composite anode shows dendrite-free Li deposition and promotes highly reversible Li plating/stripping behavior. As a result, it demonstrates excellent cycling stability for more than 1000 hours even under ultra-high rate (10 mA cm^{-2}) and high areal capacity (3 mAh cm^{-2}). More importantly, the well-designed 2D layered structure is found to be ultra-stable in the LiPS solutions due to the protection by aligned 2D nanosheets. Therefore, in the Li–S batteries, the composite Li anode is highly efficient to block the shuttled LiPSs and inhibit the corrosion of the lithium metal anode (Scheme 1). By coupling a conventional carbon/sulfur cathode with the above composite Li anode, the assembled Li–S battery exhibits a stable cycling stability of 64.5% capacity retention with a high Coulombic efficiency of 99.8% over 300 cycles. This work provides us valuable insight on the design strategies of Li metal anode in Li–S batteries.

2. Results and Discussion

Figure 1a shows the fabrication of the rGO/ $Ti_3C_2T_x$ membrane infused with molten Li metal as a composite anode (Li-rGO/

$Ti_3C_2T_x$). The GO and $Ti_3C_2T_x$ colloids suspended in water were vacuum filtered to form the densely stacked GO/ $Ti_3C_2T_x$ composite membranes (more details in the Experimental Section). The water between the interlayer was then removed by a subsequent drying process at 100°C for 6 h. Figure 1b presents the digital photo and cross-section SEM image of the as-prepared membrane, which is as thin as $7 \mu\text{m}$ with high compactness, good tenacity and excellent mechanical properties. The thickness, shape and size of the membrane are controllable due to its good machinability, which make it compatible in different battery configurations.

Prior to the Li infusion into the layered spaces, the densely stacked GO/ $Ti_3C_2T_x$ membrane is first expanded by shallowly contacting the edge of membrane with the molten Li at 200°C under the Ar atmosphere, during which the residual water is superheated and the surface functional groups are removed.^[13] The expansion is related to the vapor removal and local explosion triggered by the highly reductive molten Li.^[14] The left panel of Figure 1c shows the cross-section SEM image of the expanded membrane with gaps of several hundred nanometers between the sheets. The expansion implements no damage on the well-mixed structure of the two components, as verified by the cross-sectional EDS mappings with uniform distribution of C, Ti, and O elements in the membrane (right panel of Figure 1c). The FTIR spectra in Figure 1d show significantly weakened characteristic peaks of $-\text{OH}$ (the broad peak beyond $3,000 \text{ cm}^{-1}$), C=O ($\sim 1,730 \text{ cm}^{-1}$), $\text{C}-\text{O}-\text{C}$ ($\sim 1,045 \text{ cm}^{-1}$), and $\text{C}-\text{O}$ ($\sim 1,378 \text{ cm}^{-1}$) groups for the membranes after a capillary-force-assisted infusion process by molten Li, demonstrating the effective reduction of GO to obtain the Li-rGO/ $Ti_3C_2T_x$ membrane. Figure 1e shows the Li-rGO/ $Ti_3C_2T_x$ membrane with much enlarged thickness of $130 \mu\text{m}$ and well maintained square-shape. The membrane is filled with $\sim 93 \text{ wt. \% Li}$ in a layer-by-layer order as shown in the enlarged cross-sectional SEM image (Figure S1), demonstrating the lithiophilic nature of the rGO/ $Ti_3C_2T_x$ composite. The X-ray diffraction (XRD)



Scheme 1. The well-aligned rGO/ $Ti_3C_2T_x$ layered structure guides uniform Li growth and inhibits the corrosion of Li anode by LiPSs. a) Scheme for the shuttle of LiPSs from sulfur cathode to Li anode. b) Dendrite formation and anode corrosion by LiPSs for a bare Li anode. c) Dendrite-free Li growth and LiPSs inhibiting for the Li-rGO/ $Ti_3C_2T_x$ composite anode.

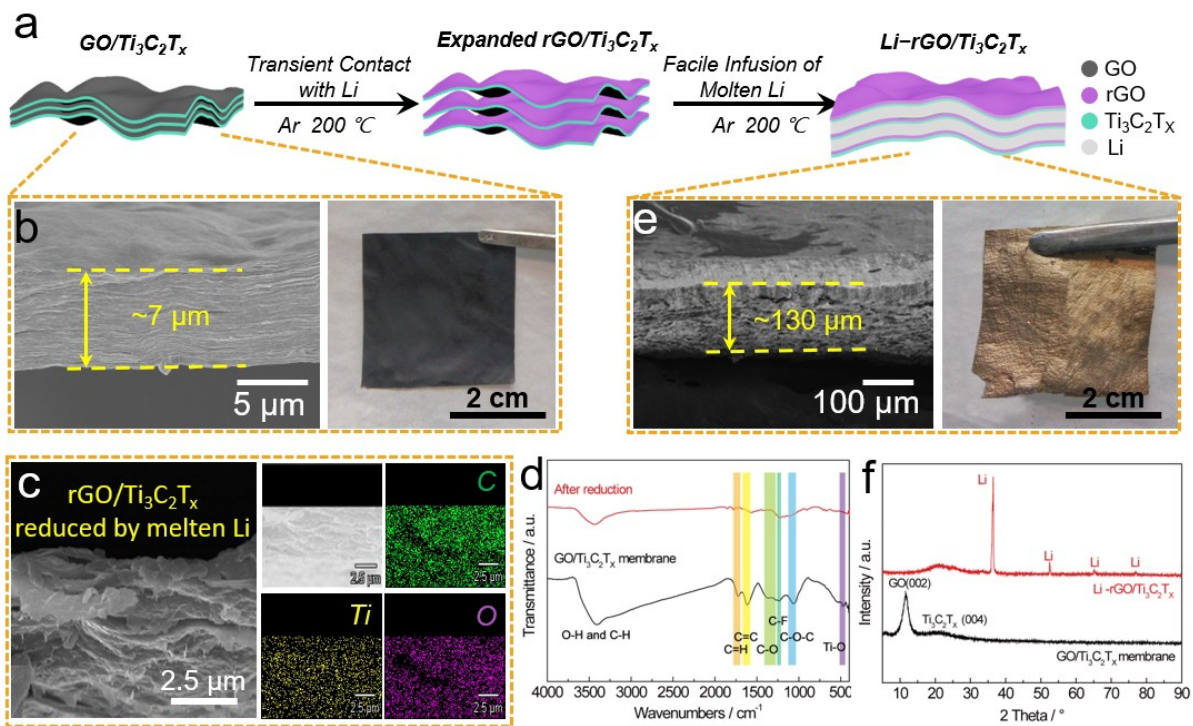


Figure 1. Preparation of Li-rGO/Ti₃C₂T_x composite anode and the structural characterizations. a) Scheme for the preparation of layered Li-rGO/Ti₃C₂T_x composite anodes. b) Cross-section SEM image and optical image of the GO/Ti₃C₂T_x membrane. c) Cross-section SEM image and EDS mapping images (C, Ti and O) of the rGO/Ti₃C₂T_x membrane. d) FTIR spectra of the GO/Ti₃C₂T_x membrane and the one after reduction. e) Cross-section SEM image and optical image of the Li-rGO/Ti₃C₂T_x composite membrane. f) XRD patterns of the GO/Ti₃C₂T_x and Li-rGO/Ti₃C₂T_x membranes.

patterns of the Li-rGO/Ti₃C₂T_x only show new peaks indexed as metallic Li comparing with the patterns of rGO/Ti₃C₂T_x (Figure 1f). Most of the entrapped Li species are not oxidized or reacting with the membrane. In the patterns of rGO/Ti₃C₂T_x, a weak (002) peak corresponding to graphene oxide indicates the incomplete reduction of GO during the expansion treatment, while it disappears after Li infusion by the further reduction of Li. Notably, the Li infusion process does not alter the crystal structure and surface chemistry of Ti₃C₂T_x nanosheets, as evidenced by the XRD patterns, FTIR spectra and the elemental mapping (Figure 1c, d and f).^[15]

The electrochemical plating/stripping of Li in the Li-rGO/Ti₃C₂T_x composite was investigated by a symmetric cell configuration. The composite electrode delivers a full Li stripping capacity of 3,231 mAh g⁻¹ (Figure S2), implying that the rGO/Ti₃C₂T_x does not compromise the high capacity merit of Li metal-based anode. For comparison, Li-rGO composite electrodes were prepared through the same procedure with that of Li-rGO/Ti₃C₂T_x by infusing Li into reduced-GO membranes (Figure S3). Symmetrical cells with Li-rGO/Ti₃C₂T_x, Li-rGO and bare Li electrodes were assembled, respectively. 1 M LiNO₃-free bis(trifluoromethane)sulfonimide lithium salt (LiTFSI) dissolved in a mixed solvent of 1, 2-dioxolane (DOL) and dimethoxymethane (DME) (1:1 by volume) was used as electrolyte here. At the current density of 4 mA cm⁻² with an areal capacity of 0.6 mAh cm⁻², the cell with Li foil electrodes displays fast increased overpotential from 138 mV to 2 V after only 30 h (113

cycles), which is caused by the uneven Li growth and the interfacial instability (Figure 2a and Figure S4). Introducing a blocking scaffold can greatly improve the cycling stability, as revealed by the red and blue traces in Figure 2a. The Li-rGO/Ti₃C₂T_x and Li-rGO composite electrodes show much lower overpotentials of ~98 and ~148 mV over 100 h respectively. The voltage hysteresis of the Li-rGO/Ti₃C₂T_x cell is lower than that of Li-rGO, indicating the smaller resistance of the as-prepared rGO/Ti₃C₂T_x host. The electrochemical impedance spectra (EIS) were further used to examine the interfacial resistance of the symmetrical cells (Figure 2b, S5, Table S1). The measurements are conducted on pristine electrodes and those after 10 cycles. In both cases, the Li-rGO/Ti₃C₂T_x cells show the lowest interface impedance as identified by the smallest radius of the semi-circles. Compared to the charge-transfer resistance of 9.84 Ω for bare Li symmetric cell, the Li-rGO/Ti₃C₂T_x cell shows the smallest charge-transfer resistance of 5.32 Ω, indicating its ease for Li plating/stripping due to the rGO/Ti₃C₂T_x interface. For the bare Li electrode, the continuous loss of dead Li and repeated crack-reformation of solid-electrolyte-interphase (SEI) lead to a resistant layer on the surface, as illustrated in the SEM images of Figures S6. The uneven surface deteriorates the growth of dendritic lithium that may penetrate the separator,^[16] and finally leads to the short-circuit. In contrast, the surface of the Li-rGO/Ti₃C₂T_x electrode presents its pristine morphology without any dendrites or dead Li, thus resulting in a longer cycle life.

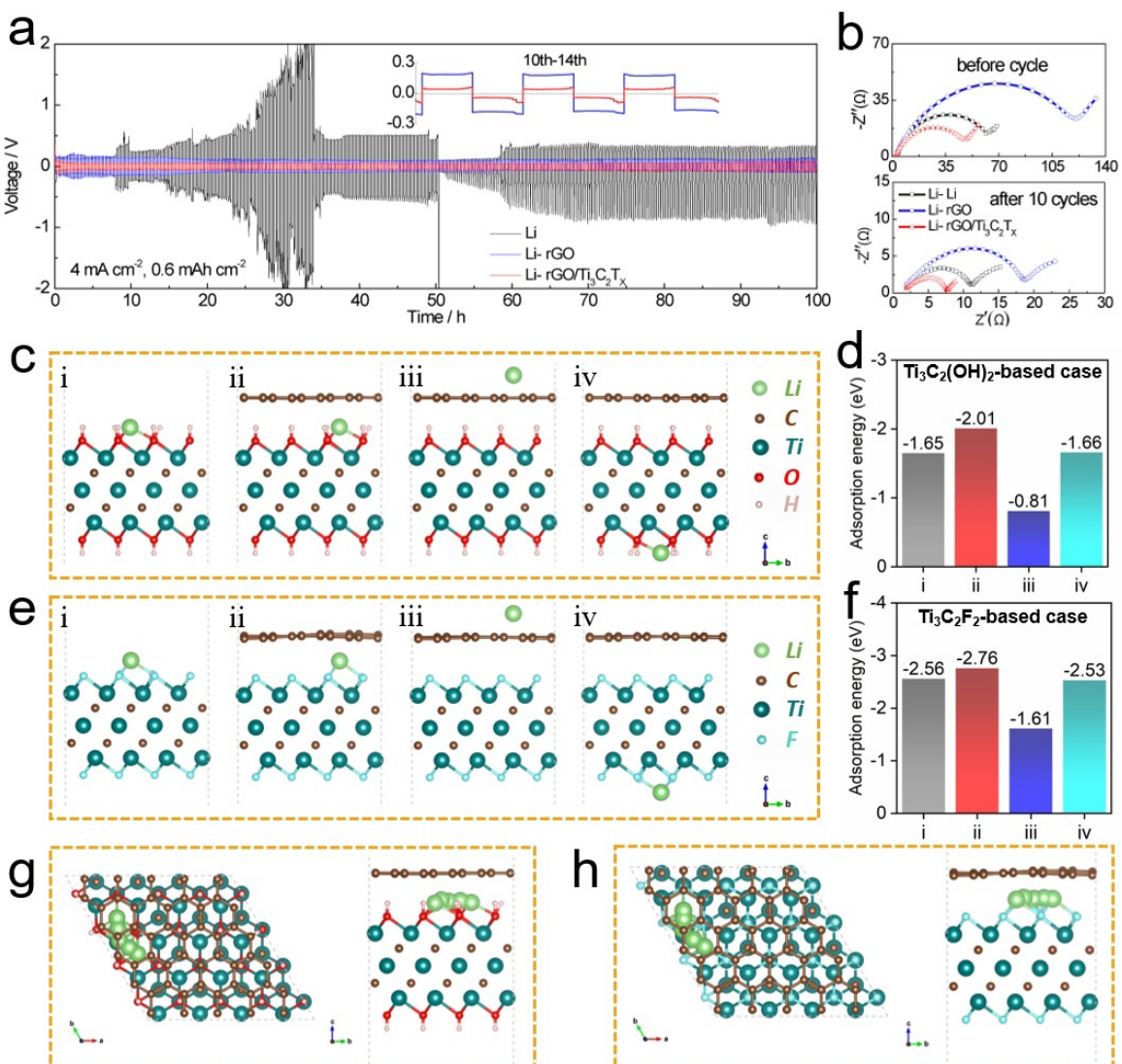


Figure 2. Cyclic stability unraveled by the theoretical computations. a) Cycling performance of symmetric cells with Li-rGO/Ti₃C₂T_x, Li-rGO and bare Li anodes under the current density of 4 mA cm⁻² and the capacity of 0.6 mAh cm⁻² condition. b) EIS plots for the symmetric cells with Li-rGO/Ti₃C₂T_x, Li-rGO and bare Li electrodes before cycling and after 10 cycles under 4 mA cm⁻² with an areal capacity of 0.6 mAh cm⁻². c) The configurations for lithium atom adsorbed on pristine Ti₃C₂(OH)₂ (i), inner side (ii), graphene-outer side (iii), and Ti₃C₂(OH)₂-outer side (iv) of graphene/Ti₃C₂(OH)₂. d) Corresponding adsorption energies for Li atom at different sites of graphene/Ti₃C₂(OH)₂. e) The configurations for lithium atom adsorbed on pristine Ti₃C₂F₂ (i), inner side (ii), graphene-outer side (iii), and Ti₃C₂F₂-outer side (iv) of graphene/Ti₃C₂F₂. f) Corresponding adsorption energies for Li atom at different sites of graphene/Ti₃C₂F₂. g-h) Diffusion pathways for Li atom at the inner sides of graphene/Ti₃C₂(OH)₂ (g) and graphene/Ti₃C₂F₂ (h).

We then investigate the underlying mechanism for the rGO/Ti₃C₂T_x (T = -OH, -F) composite as Li metal host by theoretical computations based on the density functional theory (DFT). The structural optimizing for the graphene/Ti₃C₂T_x models suggests distances of 2.19 Å and 3.02 Å between the graphene/Ti₃C₂(OH)₂ and graphene/Ti₃C₂F₂ layers, which ensure adequate space for accommodating Li atoms (Figure S7). We then examine the adsorption energies (E_a) for Li atoms at different sites of Ti₃C₂T_x or graphene/Ti₃C₂T_x (Figures 2c, 2e, S8 and S9). A higher E_a value suggests a stronger interaction between the Li atom and the substrates. As expected, the largest E_a values of -2.01 eV and -2.76 eV appear at the interface of graphene/Ti₃C₂T_x (Subgraphs ii) comparing with the

ones at the pristine Ti₃C₂T_x layers (Subgraphs i), the graphene-outer sides (Subgraphs iii), or the Ti₃C₂T_x-outer sides (Subgraphs iv) of graphene/Ti₃C₂T_x (the detailed values are plotted in Figures 2d and 2f). A more in-depth analysis for the charge transfer between Li and the substrates is carried out using the Bader charge. Taking the OH-functionalized MXene for an example, the charge transfer of Li to Ti₃C₂(OH)₂ is 0.67 e⁻ while the value is much higher for Li to the interface of graphene/Ti₃C₂(OH)₂ (0.86 e⁻), which affords higher adsorption strength to anchor Li atoms (Figure S10). The results indicate the interfaces between rGO and Ti₃C₂T_x in the rGO/Ti₃C₂T_x composite is the preferential sites for Li deposition, which promote the immobilization and enhance the utilization efficiency for Li

metal. The diffusion barriers of lithium atoms in the interlayers of graphene/Ti₃C₂T_x are calculated to evaluate the kinetics property, which present values of 0.36 and 0.19 eV for graphene/Ti₃C₂(OH)₂ and graphene/Ti₃C₂F₂ cases, respectively (Figure 2g, h). The barriers are lower than that in the graphene case reported earlier,^[66,17] which may decipher the lower voltage hysteresis of the Li-rGO/Ti₃C₂T_x electrode than that of Li-rGO as shown in Figure 2a.

The Li-rGO/Ti₃C₂T_x electrodes were further cycled under harsher conditions. The superior rate performance of Li-rGO/Ti₃C₂T_x are verified by the Li plating/stripping tests at different current densities (Figures 3a and S11), demonstrating the better rate performance of the composite Li anode. As shown in Figure 3b, the composite electrodes maintain a long-term cycling stability under 10 mA cm⁻²/³ mA h cm⁻² with the overpotential keeping stable at ~114 mV for 1000 h (inset of Figure 3b). By comparison, the voltage profiles of the bare Li cell show severe voltage fluctuation with the obviously increased overpotentials from ~80 mV to ~150 mV (Figures 3b and S12). A short-circuit occurs after 300 h cycling due to the aggregation of dendrites and dead Li on the anode surface. Besides, the voltage plateaus remains stable for Li-rGO/Ti₃C₂T_x cell during the entire operation of Li plating/stripping, which are closely related to the variation of the electrode surface during cycling.^[18] The as-prepared Li-rGO/Ti₃C₂T_x composite

anode presents excellent stability under high current and high capacity conditions, as compared with the reported lithium composite host (Table S2). Post-test SEM characterizations were conducted for the electrodes after 10 cycles under 10 mA cm⁻²/³ mA h cm⁻² condition. The bare Li electrode presents a mossy surface after cycling (Figure 3d) and obvious dendrite deposition is observed in the cross-section SEM image (Figure 3e). Benefiting from the outstanding lithophilic property at the interface of rGO and Ti₃C₂T_x, the Li among Li-rGO/Ti₃C₂T_x electrode is well confined in the well-aligned layers, showing a smoother surface before and after cycling, (Figures 3f–3h). The folded rGO/Ti₃C₂T_x sheets in Figure 3g uncover the deposited Li underneath the thin layer. Cross-section image of the electrode also exhibits the flat morphology without any dendrites (Figure 3h). The overall side-views of the fresh Li-rGO/Ti₃C₂T_x electrode (Figure 3i) and the one after 10 cycles (at the stripping state, Figure 3k) show the good integrity of the rGO/Ti₃C₂T_x scaffold (Figure S13). After stripping, the pristine layered Li (Figure 3j) is removed and the gaps in the rGO/Ti₃C₂T_x host appear again, with SEI species covering on the surface. These results suggest that the rGO/Ti₃C₂T_x membrane is an excellent host to enable reversible Li plating/stripping.

To demonstrate the advantages of such composite anode in Li–S batteries, the stability of bare Li and Li-rGO/Ti₃C₂T_x against the LiPS corrosion is compared by soaking them in the

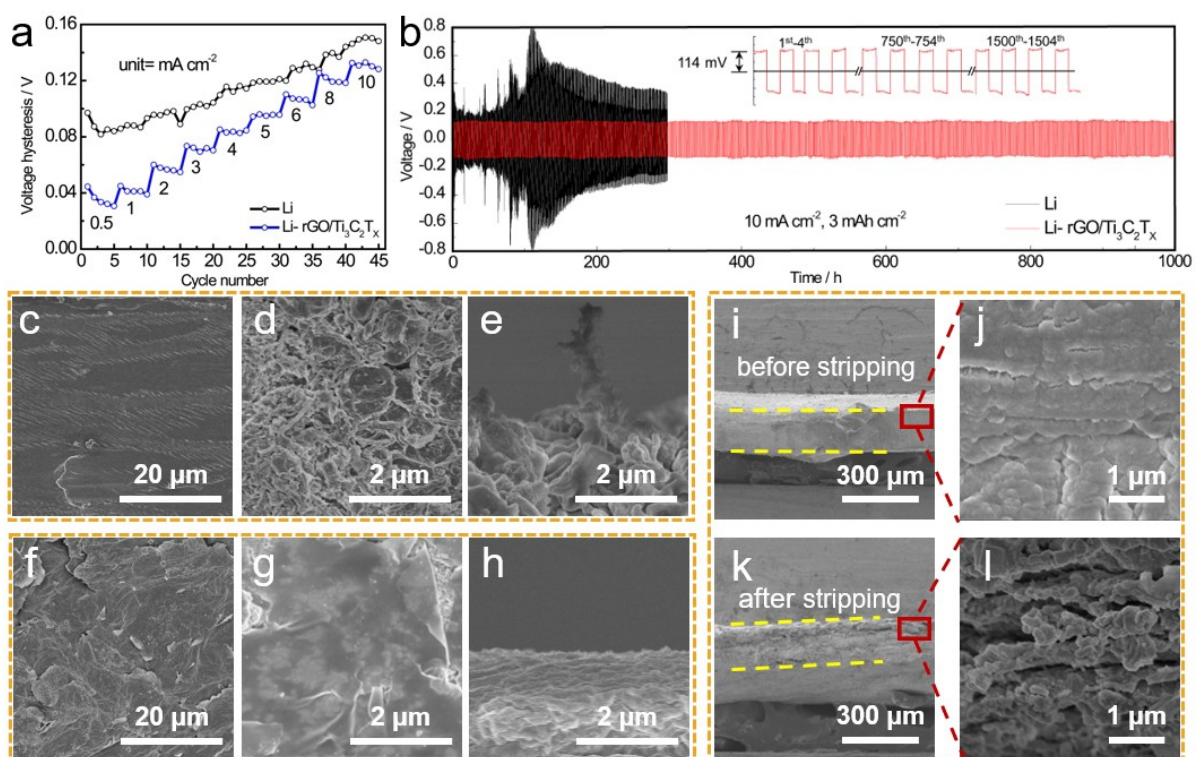


Figure 3. Morphology evolution of bare Li and Li-rGO/Ti₃C₂T_x during the Li plating/stripping process. a) Voltage hysteresis of the Li plating-stripping process for Li-rGO/Ti₃C₂T_x and bare Li electrodes under different current densities. b) Long-term cycling performance of symmetric cells with Li-rGO/Ti₃C₂T_x and bare electrodes under 10 mA cm⁻²/³ mA h cm⁻² condition. c) SEM image of fresh Li surface. d) Top-view and e) cross-section SEM images of bare Li electrode after 10 cycles under 10 mA cm⁻²/³ mA h cm⁻² condition. f) SEM image of fresh Li-rGO/Ti₃C₂T_x surface. g) Top-view and h) cross-sectional SEM images of the Li-rGO/Ti₃C₂T_x electrode after 10 cycles under 10 mA cm⁻²/³ mA h cm⁻² condition; i–j) Cross-section SEM images of the fresh Li-rGO/Ti₃C₂T_x electrode; k–l) SEM images at the Li stripped state after 10 cycles under 10 mA cm⁻²/³ mA h cm⁻² condition.

0.5 M Li₂S₆-DME solution. The pristine Li₂S₆-DME solution is light yellow, which will change to dark red or brown if long-chain soluble LiPSs are formed. In Figure 4a, bare Li metal in the Li₂S₆ solution promotes the formation of long-chain LiPSs as identified by the darker color. In contrast, the solution with the Li-rGO/Ti₃C₂T_x maintains its color during 1 week of standing (Figure 4b), demonstrating the remarkable stability of the composite Li anode against the corrosion by LiPSs. The corrosion between LiPSs and Li anode will produce Li₂S₂ and Li₂S solids covered on the anode surface. The soaked Li anodes were taken out after 1 week and washed with pure DME. The SEM image of the soaked bare Li electrode shows noticeable deposition of sulfide species (Figure 4c). In contrast, the Li-rGO/Ti₃C₂T_x electrode exhibits a smooth surface without obvious deposition of foreign matters (Figure 4d), further confirming its stability against LiPS corrosion. The stability of Li anode in LiPS electrolyte is vital to ensure the efficient operation of Li-S cells.

We then prepared CMK-3/sulfur cathodes (Figure S14)^[19] and coupled them with bare Li or Li-rGO/Ti₃C₂T_x anodes to assemble Li-S full cells. The cells were activated by 4 charge/discharge cycles at 0.2 C (1 C = 1675 mAh g⁻¹) and then cycled at 1 C (Figures 4e and S15). The bare Li cell and Li-rGO/Ti₃C₂T_x cell show initial capacities of 1093 and 1070 mAh g⁻¹. At the higher current density of 1 C, Li-rGO/Ti₃C₂T_x cell exhibits a specific capacity of 634 mAh g⁻¹ and maintains high capacity retention of 64.5% at 409 mAh g⁻¹ after 300 cycles. However, the bare Li cell only retains 29.6% with a much lower specific capacity of 178 mAh g⁻¹ after 300 cycles. Moreover, the Coulombic efficiency (CE) with the Li-rGO/Ti₃C₂T_x anode is highly stable with an average of 99.8%, demonstrating the effective utilization of the cathode materials along with the cycling. The unstable

Coulombic efficiency of the bare Li cell is attributed to the irreversible side reactions between LiPSs and the Li anode. The soluble LiPSs tend to shuttle to the Li anode and be reduced by the bare Li, with the solid products (Li₂S or Li₂S₂) covering on the anode surface (Figure 4c and 4f). By comparison, the rGO/Ti₃C₂T_x host is highly efficient to block the shuttled polysulfides and inhibit the corrosion of the Li anode, resulting in stable coulombic efficiency and cycling performance (Figure 4e).

In contrast, the cell with the bare Li anode presents low average CE of ~92%, which is attributed to the irreversible side reactions between LiPSs and the Li anode.^[20] The Li₂S/Li₂S₂ products are agglomerated on the anode surface, which block Li⁺ ion transport and passivate the Li anode.^[21] After 300 cycles, the bare Li presents a severely corroded surface with large cracks and irregular particles as observed from Figures 4f. The rough surface provides more contact between the dissolved LiPSs and Li,^[21b] which further leads to a deeper corrosion of the anode during the repeated cycles. The low-magnification SEM image shows the extensive corrosion among the bare Li anode (Figure S16a), but the Li-rGO/Ti₃C₂T_x anode presents a much smoother and denser surface. These results indicate that the rGO/Ti₃C₂T_x scaffold effectively suppress the corrosion of Li anode by LiPSs species, promoting a highly stable cycling performance in Li-S batteries.

3. Conclusions

We have demonstrated a layered Li-rGO/Ti₃C₂T_x composite anode as an efficient polysulfide inhibitor for Li-S batteries. By combining the experimental results and theoretical computa-

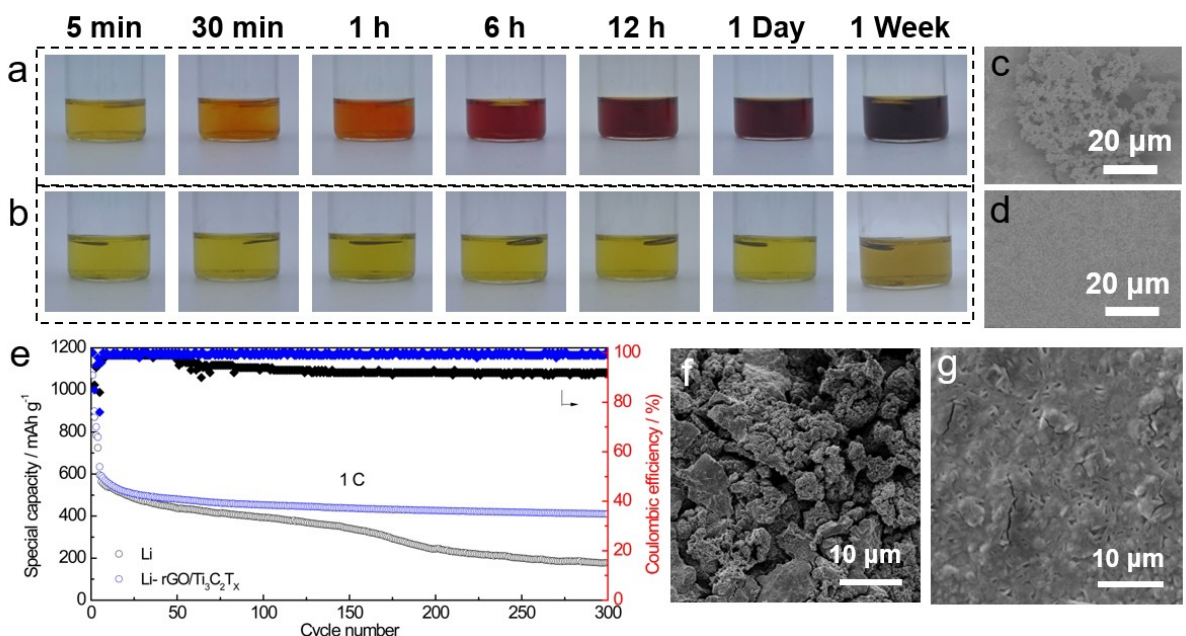


Figure 4. The layered rGO/Ti₃C₂T_x as an efficient LiPS inhibitor for stable Li-S batteries. a) Optical images of bare Li and b) Li-rGO/Ti₃C₂T_x electrodes soaked in 0.5 M Li₂S₆/DME solution for different durations from 5 min to 1 week. c) SEM images of the soaked Li and d) Li-rGO/Ti₃C₂T_x electrodes after 1 week. e) Cycling performance of Li-S cells with bare Li metal and Li-rGO/Ti₃C₂T_x anodes. f) SEM images of bare Li and g) Li-rGO/Ti₃C₂T_x electrodes after 300 charge-discharge cycles in the Li-S cells.

tions, we have found that the interface between $\text{Ti}_3\text{C}_2\text{T}_x$ and rGO is able to guide uniform Li nucleation and dendrite-free deposition, promoting highly reversible Li stripping/plating behavior. Such the composite anode demonstrates excellent cycling stability for more than 1000 hours even under ultra-high rate (10 mA cm^{-2}) and high areal capacity (3 mAh cm^{-2}). More importantly, the well-designed 2D layered structure is ultra-stable in the LiPS solutions due to the protection by the aligned 2D nanosheets. Therefore, in the Li–S batteries, the composite Li anode is highly efficient to block the shuttled LiPSs and inhibit the corrosion of the lithium metal anode. By coupling the composite anode with a conventional carbon/sulfur cathode, the Li–S battery exhibits a stable cycling stability of 64.5% capacity retention with a high CE of 99.8% over 300 cycles. This work suggests the design strategy of Li metal anode especially targeting at sulfur cathode, and we hope it can provide valuable inspirations for the future design of Li metal anodes for more practical Li–S batteries.

Experimental Section

Preparation of Li-rGO/ $\text{Ti}_3\text{C}_2\text{T}_x$ Electrodes

The colloidal suspension of graphene oxide (GO) in de-ionized water (2 mg mL^{-1}) was prepared by ultrasonication of GO powders made by modified Hummers' method. The $\text{Ti}_3\text{C}_2\text{T}_x$ colloidal suspension in water (2 mg mL^{-1}) was synthesized from Ti_3AlC_2 etched by a mixture of hydrochloric acid (HCl) and lithium fluoride (LiF). The above two suspensions were mixed by ultrasonication with a volumetric ratio of 4:1, which were filtrated under vacuum and then dried at 100°C for 6 h to obtain the GO/ $\text{Ti}_3\text{C}_2\text{T}_x$ composite films. Before the molten Li infusion, a spark reaction was performed on the GO/ $\text{Ti}_3\text{C}_2\text{T}_x$ film by shallowly contacting its edge with the molten Li at 200°C in an argon-filled glove box with sub-ppm O_2 level. GO was simultaneously reduced to rGO by the thermal reduction process. Li-rGO/ $\text{Ti}_3\text{C}_2\text{T}_x$ composite electrodes were then prepared by further contacting the edges of the rGO/ $\text{Ti}_3\text{C}_2\text{T}_x$ films with the molten Li on a nickel foil heated to 200°C . Li-rGO composite electrodes were synthesized by the same procedure except for adding $\text{Ti}_3\text{C}_2\text{T}_x$.

Preparation of CMK-3/S Cathodes

CMK-3/S cathode was prepared by a simple melt-diffusion method. Sulfur powders (99.5%, Aladdin) and CMK-3 (XFNANO Materials Tech Co., Nanjing, China) with a mass ratio of 7:3 were mixed and milled uniformly. The mixture was heated in a muffle furnace at 160°C for 12 h. The CMK-3/S hybrid, carbon nanotubes and polyvinylidene fluoride (PVDF) with a mass ratio of 8:1:1 were mixed and dispersed in N-methyl pyrrolidinone (NMP) to form a homogeneous slurry, which was then coated onto a carbon-coated aluminum foil and dried at 60°C overnight to obtain the CMK-3/S electrode. The areal mass loading of S was about 1 mg cm^{-2} .

Material Characterization

The morphology of the samples was captured by scanning electron microscopy (SEM, Hitachi S4800) with an accelerating voltage of 3.0 kV. Transmission electron microscopy (TEM, JEM 3100F, JEOL Co. Ltd) characterization was operated at 200 kV. X-ray diffraction (XRD) patterns were recorded on a Bruker D-8 (Cu Ka radiation, $\lambda =$

1.54056 \AA) and the data was collected from 5° to 90° with a scan rate of $10^\circ \text{ min}^{-1}$. Fourier transform infrared (FTIR) spectroscopy was performed on a Nicolet iS50 instrument.

Electrochemical Measurements

CR2032-type coin cells were assembled in an Ar-filled glove box. Symmetric cells were assembled with two circular pieces (12 mm in diameter) of Li-rGO/ $\text{Ti}_3\text{C}_2\text{T}_x$, Li-rGO or bare Li as electrodes. The polypropylene Celgard 2500 were used as separators. The electrolyte was 1 M bis(trifluoromethane)sulfonamide lithium salt (LiTFSI) dissolved in a mixture of 1, 2-dioxolane (DOL) and dimethoxymethane (DME) (1:1 by volume). The cells were examined on a battery analyzer (Neware Technology Co.) by galvanostatic cycling at current densities from 0.5 to 10 mA cm^{-2} with cutoff capacities of 0.6 or 3 mAh cm^{-2} . The electrochemical impedance spectroscopy (EIS) measurements were conducted using a Biologic SP-150 electrochemical workstation in a scanning frequency range from 100 kHz to 100 mHz with an AC amplitude of 10 mV. For the assembly of Li–S battery, Li-rGO/ $\text{Ti}_3\text{C}_2\text{T}_x$ or bare Li foil were used as anodes by coupling the above CMK-3/S as the cathodes. The electrolyte loaded in the cells is with an electrolyte/sulfur (E/S) ratio of ~ 15 . Four charge/discharge cycles at 0.2 C ($1 \text{ C} = 1675 \text{ mA g}^{-1}$ based on the mass of S) were performed to activate the electrode prior to long-term cycling at 1 C . An overloaded electrolyte amount with electrolyte/sulfur mass ratio of ~ 15 was employed to assemble the Li–S batteries. An excessive electrolyte loading can eliminate the influence of electrolyte and sulfur cathode on the battery performance, and hence highlight the effect of different Li anodes on the cyclic stability. For post-test SEM characterizations, the disassembled electrodes were rinsed with DME and then vacuum dried in the antechamber of the glove box.

Theoretical Computations

All theoretical calculations in this work were carried out using density functional theory (DFT) method as implemented in the VASP code. The electronic exchange-correlation energy was modelled using the Perdew-Burke-Ernzerhof (PBE) functional within the generalized gradient approximation (GGA). The projector augmented wave (PAW) method was used to describe the ionic cores. For the plane-wave expansion, a 400 eV kinetic energy cut-off was used. The convergence criterion for geometry optimizations was set to be 0.01 eV \AA^{-1} on force. The DFT-D3 empirical correction was used to describe van der Waals interactions.

Acknowledgements

The authors appreciate the support from the National Natural Science Foundation of China (Nos. 51932005 and 51972228), and the National Science Foundation of Tianjin, China (No. 18JCQNJC02300).

Conflict of Interest

The authors declare no conflict of interest.

Keywords: $\text{Ti}_3\text{C}_2\text{T}_x$ · reduced graphene oxide · interfaces · Li metal anodes · Li–S batteries

- [1] a) M. Wild, L. O'Neill, T. Zhang, R. Purkayastha, G. Minton, M. Marinescu, G. J. Offer, *Energy Environ. Sci.* **2015**, *8*, 3477; b) R. Fang, S. Zhao, Z. Sun, W. Wang, H.-M. Cheng, F. Li, *Adv. Mater.* **2017**, *29*, 1606823.
- [2] a) A. Manthiram, Y. Fu, Y.-S. Su, *Acc. Chem. Res.* **2013**, *46*, 1125; b) D. Bresser, S. Passerini, B. Scrosati, *Chem. Commun.* **2013**, *49*, 10545; c) R. Fang, S. Zhao, Z. Sun, D. W. Wang, H. M. Cheng, F. Li, *Adv. Mater.* **2017**, *29*, 1606823.
- [3] a) C. Yan, X. Q. Zhang, J. Q. Huang, Q. B. Liu, Q. Zhang, *Trends in Chem.* **2019**, *1*, 693; b) Y. He, Z. Chang, S. Wu, H. Zhou, *J. Mater. Chem. A* **2018**, *6*, 6155; c) S. S. Zhang, *J. Power Sources* **2013**, *231*, 153; d) Z. Cheng, H. Pan, H. Zhong, Z. Xiao, X. Li, R. Wang, *Adv. Funct. Mater.* **2018**, *28*, 1707597.
- [4] a) L. Ji, M. Rao, H. Zheng, L. Zhang, Y. Li, W. Duan, J. Guo, E. J. Cairns, Y. Zhang, *J. Am. Chem. Soc.* **2011**, *133*, 18522; b) D. Liu, C. Zhang, G. Zhou, W. Lv, G. Ling, L. Zhi, Q.-H. Yang, *Adv. Sci.* **2017**, *5*, 1700270; c) T. Zhou, W. Lv, J. Li, G. Zhou, Y. Zhao, S. Fan, B. Liu, B. Li, F. Kang, Q.-H. Yang, *Energy Environ. Sci.* **2017**, *10*, 1694; d) Z. Xiao, L. Li, Y. Tang, Z. Cheng, H. Pan, D. Tian, R. Wang, *Energy Storage Mater.* **2018**, *12*, 252; e) H. Li, Y. Tao, C. Zhang, D. Liu, J. Luo, W. Fan, Y. Xu, Y. Li, C. You, Z.-Z. Pan, M. Ye, Z. Chen, Z. Dong, D.-W. Wang, F. Kang, J. Lu, Q.-H. Yang, *Adv. Energy Mater.* **2018**, *8*, 1703438.
- [5] J. Zheng, M. Gu, M. J. Wagner, K. A. Hays, X. Li, P. Zuo, C. Wang, J.-G. Zhang, J. Liu, J. Xiao, *J. Electrochem. Soc.* **2013**, *160*, A1624.
- [6] a) A. Jozwiuk, B. B. Berkes, T. Weiss, H. Sommer, J. Janek, T. Brezesinski, *Energy Environ. Sci.* **2016**, *9*, 2603; b) G. Li, Q. Huang, X. He, Y. Gao, D. Wang, S. H. Kim, D. Wang, *ACS Nano* **2018**, *12*, 1500; c) T.-T. Zuo, X.-W. Wu, C.-P. Yang, Y.-X. Yin, H. Ye, N.-W. Li, Y.-G. Guo, *Adv. Mater.* **2017**, *29*, 1700389; d) Q. Yun, Y. B. He, W. Lv, Y. Zhao, B. Li, F. Kang, Q. H. Yang, *Adv. Mater.* **2016**, *28*, 6932; e) Z. Liang, D. C. Lin, J. Zhao, Z. D. Lu, Y. Y. Liu, C. Liu, Y. Y. Lu, H. T. Wang, K. Yan, X. Y. Tao, Y. Cui, *Proc. Natl. Acad. Sci. USA* **2016**, *113*, 2862; f) Q. Pang, X. Liang, A. Shyamsunder, L. F. Nazar, *Joule* **2017**, *1*, 871; g) Y. Lu, Z. Tu, L. A. Archer, *Nat. Mater.* **2014**, *13*, 961; h) Z. Cheng, Z. Xiao, H. Pan, S. Wang, R. Wang, *Adv. Energy Mater.* **2018**, *8*, 1702337; i) H. Li, D. Chao, B. Chen, X. Chen, C. Chuah, Y. Tang, Y. Jiao, M. Jaroniec, S.-Z. Qiao, *J. Am. Chem. Soc.* **2020**, *142*, 2012.
- [7] M. S. Islam, C. A. J. Fisher, *Chem. Soc. Rev.* **2014**, *43*, 185.
- [8] W. Xu, J. Wang, F. Ding, X. Chen, E. Nasybulin, Y. Zhang, J.-G. Zhang, *Energy Environ. Sci.* **2014**, *7*, 513.
- [9] K. J. Harry, D. T. Hallinan, D. Y. Parkinson, A. A. MacDowell, N. P. Balsara, *Nat. Mater.* **2014**, *13*, 69.
- [10] a) D. Lin, Y. Liu, Y. Cui, *Nat. Nanotechnol.* **2017**, *12*, 194; b) H. Li, C. S. Qi, Y. Tao, H. B. Liu, D. W. Wang, F. Li, Q. H. Yang, H. M. Cheng, *Adv. Energy Mater.* **2019**, *9*, 1900079.
- [11] a) B. Anasori, M. R. Lukatskaya, Y. Gogotsi, *Nat. Rev. Mater.* **2017**, *2*, 16098; b) M. Ghiddu, M. R. Lukatskaya, M.-Q. Zhao, Y. Gogotsi, M. W. Barbour, *Nature* **2014**, *516*, 78.
- [12] a) H. Shi, C. J. Zhang, P. Lu, Y. Dong, P. Wen, Z. S. Wu, *ACS Nano* **2019**, *13*, 14308; b) B. Li, D. Zhang, Y. Liu, Y. Yu, S. Li, S. Yang, *Nano Energy* **2017**, *39*, 654; c) X. Zhang, R. Lv, A. Wang, W. Guo, X. Liu, J. Luo, *Angew. Chem. Int. Ed.* **2018**, *57*, 15028; d) Q. Z. Zhenjiang Cao, S. Wang, D. Zhang, H. Chen, Z. Du, B. Li, S. Yang, *Adv. Funct. Mater.* **2019**, *30*, 1908075.
- [13] a) Y. Gao, X. Chen, J. Zhang, H. Asakura, T. Tanaka, K. Teramura, D. Ma, N. Yan, *Adv. Mater.* **2015**, *27*, 4688; b) G. Sun, L. Zheng, Z. Zhan, J. Zhou, X. Liu, L. Li, *Carbon* **2014**, *68*, 748.
- [14] D. Lin, Y. Liu, Z. Liang, H. W. Lee, J. Sun, H. Wang, K. Yan, J. Xie, Y. Cui, *Nat. Nanotechnol.* **2016**, *11*, 626.
- [15] a) Q. Xue, H. Zhang, M. Zhu, Z. Pei, H. Li, Z. Wang, Y. Huang, Y. Huang, Q. Deng, J. Zhou, S. Du, Q. Huang, C. Zhi, *Adv. Mater.* **2017**, *29*, 1604847; b) L. Huang, T. Li, Q. Liu, J. Gu, *Electrochim. Commun.* **2019**, *104*, 106472.
- [16] a) G. Bieker, M. Winter, P. Bieker, *Phys. Chem. Chem. Phys.* **2015**, *17*, 8670; b) Y. Lu, K. Korf, Y. Kambe, Z. Tu, L. A. Archer, *Angew. Chem. Int. Ed.* **2014**, *53*, 488; c) Y. Lu, Z. Tu, L. A. Archer, *Nat. Mater.* **2014**, *13*, 961.
- [17] C. Uthaisar, V. Barone, *Nano Lett.* **2010**, *10*, 2838.
- [18] B. Duan, W. Wang, H. Zhao, A. Wang, M. Wang, K. Yuan, Z. Yu, Y. Yang, *ECS Electrochem. Lett.* **2013**, *2*, A47.
- [19] X. Ji, K. T. Lee, L. F. Nazar, *Nat. Mater.* **2009**, *8*, 500.
- [20] S. Risso, S. Angioletti-Uberti, J. Dzubiella, M. Ballauff, *J. Power Sources* **2014**, *267*, 648.
- [21] a) J.-Q. Huang, Q. Zhang, H.-J. Peng, X.-Y. Liu, W.-Z. Qian, F. Wei, *Energy Environ. Sci.* **2014**, *7*, 347; b) J. Zheng, M. Gu, H. Chen, P. Meduri, M. H. Engelhard, J.-G. Zhang, J. Liu, J. Xiao, *J. Mater. Chem. A* **2013**, *1*, 8464.

Manuscript received: March 25, 2020

Revised manuscript received: April 27, 2020

Accepted manuscript online: April 27, 2020

Version of record online: May 19, 2020